IET Power Electronics

Research Article

IET Journals
The Institution of Engineering and Technology

Analysis and behavioural modelling of matching networks for resonant-operating capacitive wireless power transfer

ISSN 1755-4535
Received on 23rd October 2018
Revised 7th January 2019
Accepted on 17th January 2019
doi: 10.1049/iet-pel.2018.6136
www.ietdl.org

Eli Abramov[1], Jose Marcos Alonso[2], Mor Mordechai Peretz[1] ✉

[1]*The Center for Power Electronics and Mixed-Signal IC, Department of Electrical and Computer Engineering, Ben-Gurion University of the Negev, P.O. Box 653, Beer-Sheva, 84105, Israel*

[2]*Electrical Engineering Department, University of Oviedo, Campus de Viesques, 33204, Gijón, Asturia, Oviedo, Spain*

✉ *E-mail: morp@bgu.ac.il*

Abstract: This study introduces a two-port network-based behavioural modelling approach for resonant-operated capacitive wireless power transfer (WPT) systems. A simple, generic and unified modelling approach is developed to describe the behaviour of WPT systems, under changes of the source and load circuits, variations of the coupling interface and drifts of the components in the matching networks. The resultant model provides insights into the electrical cross-coupling relationships between input and output parameters of the capacitive power transfer systems, including the effect of distance and alignment of the coupling plates. Regardless of the circuit complexity, it is demonstrated that the model core can be reduced to a basic gyrator relationship with added coefficients when required, thus obtaining a compact, closed-form relationship between the input and output. To provide a simulation framework for capacitive medium variations, a simulation-compatible model of the capacitive coupling using a continuous-time variable capacitor has been constructed. The behavioural model and methodology have been validated through simulations and experiments. A 200 W experimental capacitive WPT prototype has been designed and examined for various air-gaps up to 100 mm at a resonant operation of 1.56 MHz. A very good agreement is obtained between the theoretical predictions, simulations, and experimental results.

1 Introduction

As the field of mobile technology advances and adds more innovative uses, applications such as portable electronics, virtual and augmented reality, smartphones, electric vehicles, biomedical systems etc. are being used for extended periods [1–12]. In present-day portable electronics, compact power sources and interfaces are essential to keep high-performance devices, constantly accessible. In many volume-sensitive mobile or portable applications, the use of bulk batteries becomes prohibitive due to size allocations and thermal management. Wireless power transfer (WPT) technology is a growing alternative for bulk batteries as a reliable source of energy [11–17].

Capacitive power transfer (CPT) has been investigated in recent years, as an alternative near-field power transfer method to well-known magnetic-field-based approaches [1, 4, 6]. One of the more attractive advantages of capacitive-based WPT is the avoidance of undesired Eddy currents and electromagnetic interference that come with magnetic-based WPT methods. In addition to efficiency improvements, CPT systems are potential with lower volume and construction complexity [18–23]. However, the power transfer capability and efficiency still depend on the distance and alignment between the transmitting and receiving sides, which is an inherent feature of near-field WPT systems [19, 23, 24]. Several explorations and remedies for an extended range power transfer are covered in the literature [25–29], for general and CPT. An important step in the development of both uniform and specific solutions for extended range WPT systems is a generalised description of the energy transfer mechanism. This requires a description of the transfer medium, circuit behaviour and their interaction. In particular, in case that active compensation is added, a description of the system's dynamic response is essential. On the topic of magnetic-field-based WPT, there can be found several models based on circuit and system analyses, however, a generic behavioural model and modelling methodology for CPT has not been addressed hitherto.

A simplified block diagram of a descriptive CPT system is shown in Fig. 1. In a similar way to magnetic field approaches, reactive networks on both primary and secondary sides are used for impedance matching between the source and load [26–30]. To achieve suitable degrees of freedom in terms of design, performance and overall input–output relationships in any WPT system, high-order matching networks are used [19, 28–31]. Analysis of such high-order networks can be quite complex and tedious. As a result, the complex interaction between the system parameters and characteristics may be overlooked. Several approaches have been employed to decipher the operation of high-order resonant structures such as analytical multivariable matrix manipulations, geometrical representations [32, 33], and averaging [33–35]. Circuit derivation of CPT based on superposition theorem [21, 36] provides clear closed-form expressions of the power delivery and other important relationships. However, since some approximations are involved, accurate overall description is not always obtained, in particular for the description of the dynamic characteristics. Numerical simulations are also a strong tool to evaluate and characterise different resonant circuits. This approach, however, loses generality and may be time consuming for cases that a time domain cycle-by-cycle simulation for high-frequency drive signals (several MHz) is carried out [37–42]. It would be extremely beneficial if a *simple and unified generic averaging behavioural modelling methodology for capacitive-based WPT systems* is utilised, which is the goal of this study. Furthermore, a practical approach for describing and evaluating the behaviour of CPT systems establishes the core fundamentals for overall closed-loop analysis and controller design for capacitive-based WPT.

The objective of this study is, therefore, to introduce a network-based approach to describe the behaviour of capacitive WPT systems that operate in resonant conditions, under variations of the source and load circuits, coupling interface and matching networks. The modelling methodology results in a compact, closed-form, model for CPT that provides an insight into the cross-coupling relationship between the input and output parameters and enables to account for changes in the distance and alignment of the coupling plates. It is a further objective of this study to present a simulation-compatible model of the capacitive coupling by a continuous-time variable capacitor representation. This provides a simulation platform to further analyse and examine wireless CPT.

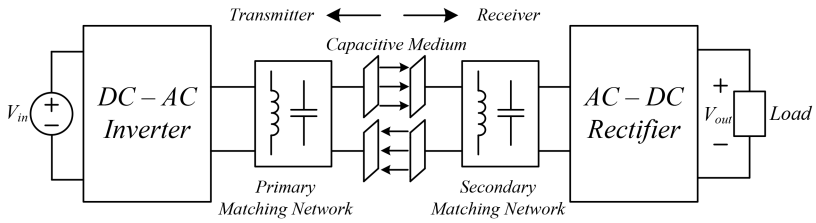

Fig. 1 *Typical diagram of capacitive WPT system*

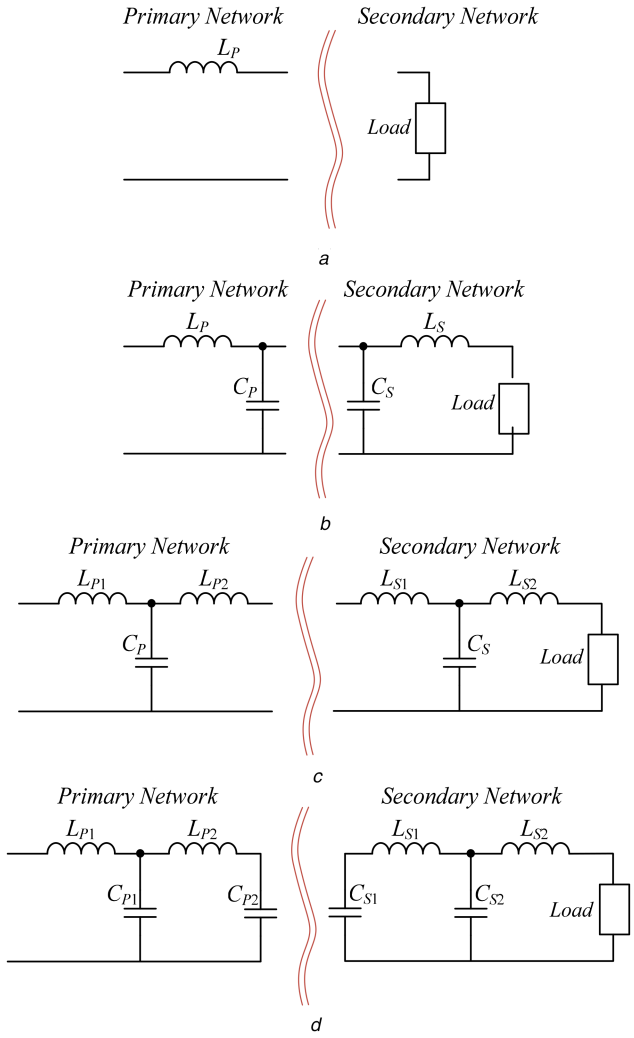

Fig. 2 *Matching networks for capacitive WPT systems*
(a) Series L, ***(b)*** Double-sided LC, ***(c)*** Double-sided LCL, ***(d)*** Double-sided LCLC

The rest of the paper is organised as follows: Section 2 briefly surveys WPT matching structures and two-port network based analysis. Section 3 presents a case study of a network-based approach to analyse a captive WPT. Section 4 describes a simulation-compatible model of capacitive coupling medium using a continuous variable capacitor. Experimental validation of the behavioural model is provided in Section 5. Finally, Section 6 concludes the paper.

2 Review: two-port representation of matching networks

A fundamental building block of various resonant conversion systems is a matching network. It typically comprises a second- or higher-order impedance that connects a sourcing circuit to a loading one. The use of these networks serves many design objectives such as reducing circulating energy in the converter [43], lower voltage and current stresses of the switches [44], assuring soft-switching over a wide range [28] etc. Particularly in WPT systems, matching networks provide additional degrees of freedom to interact between the primary and secondary circuits and compensate for resonant frequency, volt-ampere ratings, constant voltage/current output (load-independent operation), output power and system efficiency [23, 28–30]. In the following subsection, a brief review of the basic matching networks is carried out in the particular context of the capacitive wireless medium, which is then used to characterise the behaviour of a network as an energy transfer element.

2.1 Survey of selected matching networks configurations and their primary features

Fig. 2 shows several popular matching networks that are mostly used in capacitive WPT systems [18–23]. A well-known and simple option is depicted in Fig. 2*a* in which a series inductance connects to the coupling capacitance of the wireless medium and forms a resonator [18]. By this, operation in the vicinity of the resonant frequency results in efficient power transfer to the load. However, a significant drawback of this configuration is that any change either in the capacitive medium or the load parameters, even the slightest, results in different operating point and a significant deterioration of the system ability to transfer power. This is somewhat alleviated by the configuration in Fig. 2*b*, in which both the primary and secondary sides of the coupling element include series-parallel L-type resonators (also referred to as double-sided inductor–capacitor (LC)). Here, the operating frequency is near the matching network's resonance, and therefore the system is less sensitive to variations in the coupling capacitance (due to distance or misalignment variations). At the cost of slightly higher component count, the power transfer capabilities are higher than in a series compensation, but still depending on the coupling for efficiency and delivered power [21, 23].

The structure in Fig. 2*c* is a combination of the LC matching network with an additional series inductor on both sides of the system (double-sided inductor–capacitor–inductor (LCL)). By proper design of the inductors (L_P, L_{P1}, L_S, L_{S1}), this setup provides several degrees of freedom to adjust the power transfer of the system. However, as in the case of the LC matching network, the power transfer capabilities of the LCL structure is inversely proportional to the coupling capacitance [18, 20]. A more complex matching network is shown in Fig. 2*d*, which consists of a greater number of reactive elements in both primary and secondary (double-sided inductor–capacitor–inductor–capacitor (LCLC)). There, the coupling capacitance, in this case, does not directly influence the resonance of the matching networks. However, it still limits the amount of power transfer of the system, i.e. the maximum power that the system is able to transfer is proportional to the coupling capacitance [19].

2.2 Equivalent representations of matching networks

Matching L-type structures such as a series inductor combined with a parallel capacitor (series–parallel LC, Fig. 2*b*) and a parallel capacitor combined with a series inductor (parallel–series LC, Fig. 2*b*) can be described by a two-port network with gyrator characteristics [45]. A gyrator is a passive, lossless, linear two-port transformation network in which the output and input currents depend on the input and output voltages, respectively, with respect to its transconductance gain G. In circuit theory, gyrators often used to reflect inductance using capacitance, impedance into admittance, and vice versa [46–49]. The input–output relationship of an ideal gyrator as a two-port network can be expressed as

$$\begin{bmatrix} I_1 \\ I_2 \end{bmatrix} = \begin{bmatrix} 0 & -G \\ G & 0 \end{bmatrix} \begin{bmatrix} V_1 \\ V_2 \end{bmatrix}. \tag{1}$$

In the context of the above discussion, voltage and current relationships of a series–parallel LC matching structure (Fig. 3*a*) can be derived as follows:

$$\begin{cases} V_{\mathrm{P1}} = \mathrm{j}\omega L_{\mathrm{P}} I_{\mathrm{P1}} + V_{\mathrm{P2}} \\ V_{\mathrm{P2}} = \dfrac{1}{\mathrm{j}\omega C_{\mathrm{P}}}(I_{\mathrm{P1}} - I_{\mathrm{P2}}) \end{cases} \Rightarrow \begin{cases} I_{\mathrm{P1}} = \dfrac{(V_{\mathrm{P1}} - V_{\mathrm{P2}})}{\mathrm{j}\omega L_{\mathrm{P}}}. \\ V_{\mathrm{P1}} = \mathrm{j}\omega L_{\mathrm{P}} I_{\mathrm{P1}} + \dfrac{1}{\mathrm{j}\omega C_{\mathrm{P}}}(I_{\mathrm{P1}} - I_{\mathrm{P2}}). \end{cases} \tag{2}$$

Assuming operation at the resonant frequency, the currents I_{P1} and I_{P2} are given by

$$\begin{cases} I_{\mathrm{P1}} = -\mathrm{j}\omega C_{\mathrm{P}}(V_{\mathrm{P1}} - V_{\mathrm{P2}}); \\ I_{\mathrm{P2}} = \mathrm{j}\omega_0 C_{\mathrm{P}} V_{\mathrm{P1}}; \end{cases} \quad \omega_0 L_{\mathrm{P}} = \frac{1}{\omega_0 C_{\mathrm{P}}}, \tag{3}$$

where ω_0 is the resonant angular frequency.

Employing few configurational modifications to the L-type network of Fig. 3*a*, an equivalent representation can be obtained. As can be seen in Fig. 3*b*, by addition of a series resonator (whereas $L_{\mathrm{P}}^* = L_{\mathrm{P}}$ and $C_{\mathrm{P}}^* = C_{\mathrm{P}}$) the network is transformed into a T-type one (L_{P}–C_{P}–L_{P}^*) with an output series capacitance C_{P}^*. The resultant voltage and current relationships have a two-port gyrator characteristic as follows:

$$\begin{aligned} V_{\mathrm{P1}} &= \mathrm{j}\omega_0 L_{\mathrm{P}} I_{\mathrm{P1}} + \frac{1}{\mathrm{j}\omega_0 C_{\mathrm{P}}}(I_{\mathrm{P1}} - I_{\mathrm{P2}}) = -\frac{1}{-\mathrm{j}\omega_0 C_{\mathrm{P}}} I_{\mathrm{P2}}, \\ V_{\mathrm{P2}}^* &= -\mathrm{j}\omega_0 L_{\mathrm{P}} I_{\mathrm{P2}} \frac{1}{\mathrm{j}\omega_0 C_{\mathrm{P}}}(I_{\mathrm{P1}} - I_{\mathrm{P2}}) = \frac{1}{\mathrm{j}\omega_0 C_{\mathrm{P}}} I_{\mathrm{P1}}, \end{aligned} \tag{4}$$

and in a matrix representation, it can be written as

$$\begin{bmatrix} I_{\mathrm{P1}} \\ I_{\mathrm{P2}} \end{bmatrix} = \begin{bmatrix} 0 & \underbrace{\mathrm{j}\omega_0 C_{\mathrm{P}}}_{-G} \\ \underbrace{-\mathrm{j}\omega_0 C_{\mathrm{P}}}_{G} & 0 \end{bmatrix} \begin{bmatrix} V_{\mathrm{P1}} \\ V_{\mathrm{P2}}^* \end{bmatrix}, \tag{5}$$

where the transconductance gain is $G = -\mathrm{j}\omega_0 C_{\mathrm{P}}$. It should be noted that assuming operation in resonance, the addition of the series branch is an effectively short circuit and does not change the behaviour of the circuit.

Following the above observations, the series output capacitance C_{P}^* can be reflected to an input parallel inductance L_{P}^*, as shown in Fig. 3*c*. Finally, the original L-type network can be represented as a gyrator element (Fig. 3*d*) with parallel input inductance L_{P} (full mathematical derivations have been omitted here for clarity and are detailed in the Appendix).

In analogy to the above practice for the series–parallel LC matching network, the parallel–series LC structure in Fig. 4*a* can also be defined by a gyration ratio. This is facilitated by the addition of a parallel resonator (whereas $L_{\mathrm{P}}^* = L_{\mathrm{P}}$ and $C_{\mathrm{P}}^* = C_{\mathrm{P}}$) as shown in Fig. 4*b*. Similarly to the case of the series branch, the parallel resonator is an effectively open circuit when operating at resonance and does not change the original characteristics of the circuit. The L-network is transformed into a π-type one (C_{S}–L_{S}–C_{S}^*) with parallel output inductor L_{S}^*. The parallel–series LC structure can be described as a gyrator element with parallel output inductor L_{S} as shown in Fig. 4*c*.

A π-type network can also be constructed in LCL configuration as depicted in Fig. 5*a*. Under resonant conditions, the LCL π-type configuration can be directly represented as a pure gyrator (Fig. 5*b*). It should be emphasised that for the case of the LCL π-type matching network, the transconductance gain G is positive, as opposed to the analysis of the circuits in Figs. 3 and 4.

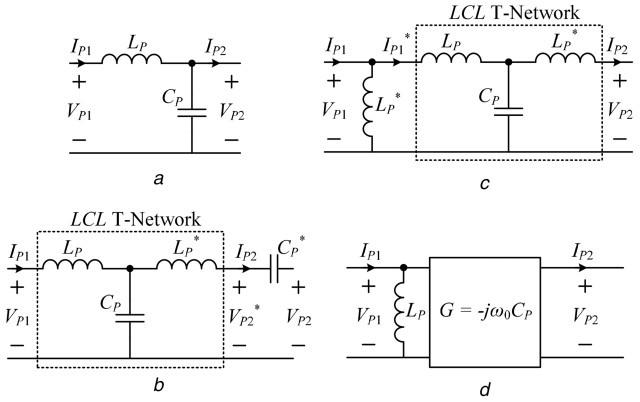

Fig. 3 *Equivalent representations of series–parallel LC matching network*
(a) L-type series-parallel resonant LC circuit, ***(b)*** Series resonator connected to the L-type circuit for T-type network arrangement, ***(c)*** Modified T-type series–parallel LC resonant circuit, ***(d)*** Two-port representation of the original L-type network

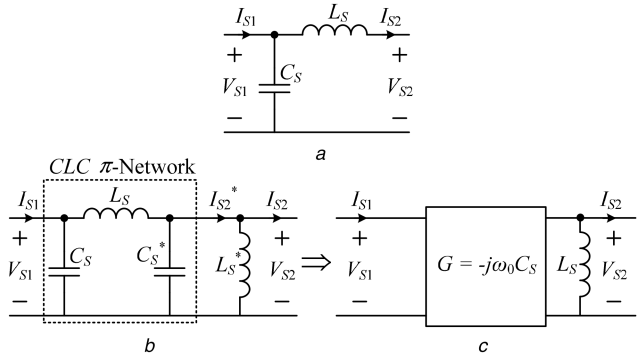

Fig. 4 *Equivalent representations of parallel–series LC matching network*
(a) L-type parallel–series resonant LC circuit, ***(b)*** Parallel resonator connected to the L-type circuit for π-type network arrangement, ***(c)*** Two-port network with gyrator characteristics

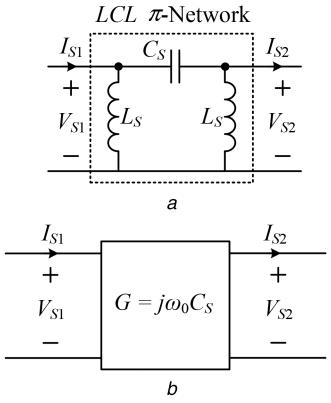

Fig. 5 *Two-port network*
(a) LCL π-type, ***(b)*** As a gyrator model

3 Case study: double-sided L-type capacitive WPT system

Following the observations and derivations made in the previous section, a capacitively-coupled power transfer system with double-sided L-type matching networks is analysed. The schematic diagram of the full system is shown in Fig. 6. This configuration has been selected for the case study demonstration since it can be employed in a variety of medium power level CPT applications [21, 23]. As can be seen in Fig. 6, the matching networks are a series–parallel LC circuit at the primary and a parallel–series LC at the secondary. The capacitive medium is modelled by a π-network, such that C_{M} is the equivalent mutual capacitance and C_{M1} and C_{M2} are the self-capacitances of the coupling plates [20, 21]. The system is driven by a full-bridge inverter on the primary side, and

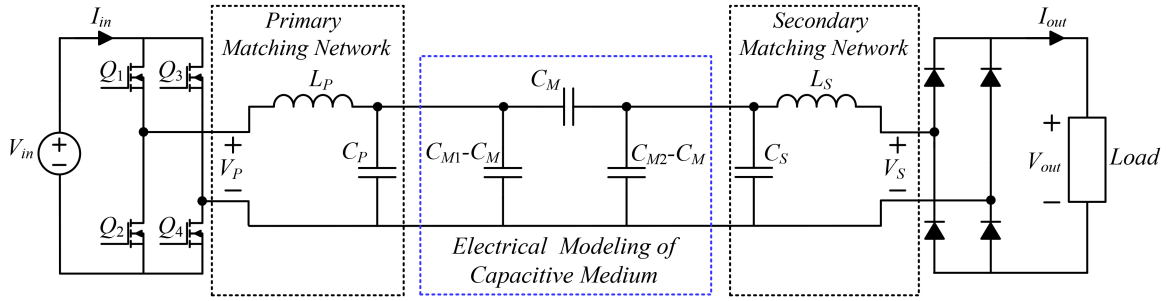

Fig. 6 *Schematic diagram of a double-sided L-type capacitive WPT system*

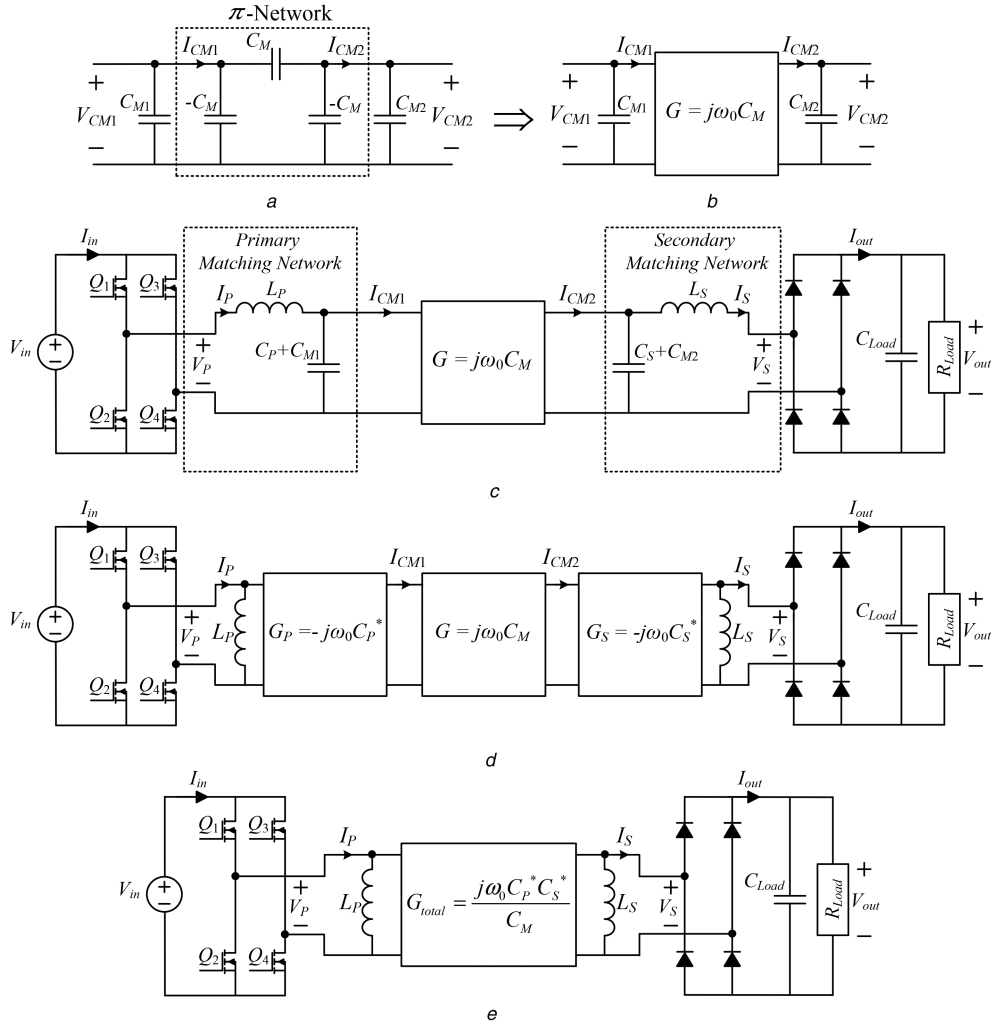

Fig. 7 *Equivalent two-port network based models of the capacitive WPT system*
(a) Electrical equivalent model of four-plate capacitive medium, ***(b)*** Representation of the capacitive medium with a two-port network, ***(c)*** Representation of double-sided L-type capacitive WPT system with a gyrator as the capacitive medium, ***(d)*** Equivalent circuit of double-sided L-type capacitive WPT system with three series gyrators, ***(e)*** Equivalent simplified circuit of double-sided L-type capacitive WPT system with a single gyrator

the load is fed via a diode rectifier that is connected to the secondary's network. Due to the structural constraints of the coupling plates, as a general practice, it is assumed that the coupling capacitance C_M is significantly lower than the total parallel capacitance. Consequently, the driving frequency is near the matching networks' resonant frequency (i.e. $f_0 = (2\pi\sqrt{L_P C_P})^{-1} = (2\pi\sqrt{L_S C_S})^{-1}$). Since the high-Q operation is naturally facilitated because of the high output impedance of the primary's network, the currents, as well as voltages of the reactive elements, are virtually sinusoidal.

For the derivations of the model, the circuit of Fig. 6 is simplified by separating the parallel capacitances of the medium from the model self-capacitances, as shown in Fig. 7*a*. This forms a π-network constructed by the mutual capacitance C_M, which can be analysed similarly to the LCL π-matching network from Section 2. This enables to use a gyrator element to represent the coupling behaviour, as depicted in Fig. 7*b*. In the context of the overall system, Fig. 6 is simplified as delineated in Fig. 7*c*. Applying the network dualities that have been established earlier, the entire system is represented by three gyrators connected in series, as shown in Fig. 7*d*, where $C_P^* = C_P + C_{M1}$ and $C_S^* = C_S + C_{M2}$; C_P, $C_S >> C_{M1}$, C_{M2}. This is further reduced to a single gyrator, as illustrated in Fig. 7*e*, with a total transconductance gain that can be expressed as

$$G_{\text{total}} = \frac{\mathrm{j}\omega_0 C_P^* C_S^*}{C_M}. \tag{6}$$

The simplified circuit of the double-sided L-type capacitive wireless power transfer system in Fig. 7*e* can be now analysed in as

a two-port network with gyrator characteristics, such that the current–voltage relationships are expressed as follows:

$$\begin{aligned} I_{\mathrm{P}} &= \frac{V_{\mathrm{P}}}{\mathrm{j}\omega_0 L_{\mathrm{P}}} - \frac{\mathrm{j}\omega_0 C_{\mathrm{P}}^* C_{\mathrm{S}}^*}{C_{\mathrm{M}}} V_{\mathrm{S}} = -\mathrm{j}\left(\frac{V_{\mathrm{P}}}{\omega_0 L_{\mathrm{P}}} + \frac{\omega_0 C_{\mathrm{P}}^* C_{\mathrm{S}}^*}{C_{\mathrm{M}}} V_{\mathrm{S}}\right), \\ I_{\mathrm{S}} &= -\frac{V_{\mathrm{S}}}{\mathrm{j}\omega_0 L_{\mathrm{S}}} + \frac{\mathrm{j}\omega_0 C_{\mathrm{P}}^* C_{\mathrm{S}}^*}{C_{\mathrm{M}}} V_{\mathrm{P}} = \mathrm{j}\left(\frac{V_{\mathrm{S}}}{\omega_0 L_{\mathrm{S}}} + \frac{\omega_0 C_{\mathrm{P}}^* C_{\mathrm{S}}^*}{C_{\mathrm{M}}} V_{\mathrm{P}}\right). \end{aligned} \tag{7}$$

From (7), the current–voltage relationships of the system are distinguished for different scenarios of (a) an asymmetrical WPT system with voltage ratings and matching networks components with different values; (b) a system with equal voltage ratings; and (c) a complete symmetrical WPT system.

For an asymmetrical system, i.e. $V_{\mathrm{P}} \neq V_{\mathrm{S}}$, $L_{\mathrm{P}} \neq L_{\mathrm{S}}$ and $C_{\mathrm{P}}^* \neq C_{\mathrm{S}}^*$ the absolute values of current–voltage relationships can be expressed in a matrix representation as follows:

$$\begin{bmatrix} I_{\mathrm{P}} \\ I_{\mathrm{S}} \end{bmatrix} = \begin{bmatrix} \dfrac{1}{\omega_0 L_{\mathrm{P}}} & \dfrac{\omega_0 C_{\mathrm{P}}^* C_{\mathrm{S}}^*}{C_{\mathrm{M}}} \\ \dfrac{\omega_0 C_{\mathrm{P}}^* C_{\mathrm{S}}^*}{C_{\mathrm{M}}} & \dfrac{1}{\omega_0 L_{\mathrm{S}}} \end{bmatrix} \begin{bmatrix} V_{\mathrm{P}} \\ V_{\mathrm{S}} \end{bmatrix}, \tag{8}$$

it should be noted that although the passive matching components are different, the resonant frequency is identical for both the primary and secondary sides.

Next, in the case that some symmetry in the form of $V_{\mathrm{P}} = V_{\mathrm{S}}$ is incorporated, however, still with different values for the matching components, then the relationship simplifies to

$$\begin{bmatrix} I_{\mathrm{P}} \\ I_{\mathrm{S}} \end{bmatrix} = \begin{bmatrix} 0 & \dfrac{1}{\omega_0 L_{\mathrm{P}}} + \dfrac{\omega_0 C_{\mathrm{P}}^* C_{\mathrm{S}}^*}{C_{\mathrm{M}}} \\ \dfrac{1}{\omega_0 L_{\mathrm{S}}} + \dfrac{\omega_0 C_{\mathrm{P}}^* C_{\mathrm{S}}^*}{C_{\mathrm{M}}} & 0 \end{bmatrix} \begin{bmatrix} V_{\mathrm{P}} \\ V_{\mathrm{P}} \end{bmatrix}. \tag{9}$$

Finally, in the particular case of a full symmetrical system, i.e. $V_{\mathrm{P}} = V_{\mathrm{S}}$, $L_{\mathrm{P}} = L_{\mathrm{S}} = L$ and $C_{\mathrm{P}}^* = C_{\mathrm{S}}^* = C$, the relationship renders down to a pure gyrator which can be expressed as

$$\begin{bmatrix} I_{\mathrm{P}} \\ I_{\mathrm{S}} \end{bmatrix} = \begin{bmatrix} 0 & \underbrace{\dfrac{1}{\omega_0 L} + \dfrac{\omega_0 C^2}{C_{\mathrm{M}}}}_{G} \\ \underbrace{\dfrac{1}{\omega_0 L} + \dfrac{\omega_0 C^2}{C_{\mathrm{M}}}}_{G} & 0 \end{bmatrix} \begin{bmatrix} V_{\mathrm{P}} \\ V_{\mathrm{S}} \end{bmatrix}. \tag{10}$$

In the typical application of this system, the operating frequency is in the MHz range, the network parallel capacitance values are in the range of hundreds of pF, inductances are tens to hundreds μH, and the mutual coupling capacitance, C_{M}, is in the order of a few pF. As a result, the transfer relationship of the system can be simplified to generic expressions as follows:

$$\begin{aligned} I_{\mathrm{P}} &= \frac{\omega_0 C_{\mathrm{P}}^* C_{\mathrm{S}}^*}{C_{\mathrm{M}}} V_{\mathrm{S}}; \\ I_{\mathrm{S}} &= \frac{\omega_0 C_{\mathrm{P}}^* C_{\mathrm{S}}^*}{C_{\mathrm{M}}} V_{\mathrm{P}}; \end{aligned} \quad \begin{cases} \dfrac{\omega_0 C_{\mathrm{P}}^* C_{\mathrm{S}}^*}{C_{\mathrm{M}}} \gg \dfrac{1}{\omega_0 L_{\mathrm{P/S}}}, \\ G \simeq G_{\mathrm{total}} = \dfrac{\omega_0 C_{\mathrm{P}}^* C_{\mathrm{S}}^*}{C_{\mathrm{M}}}, \end{cases} \tag{11}$$

which is in excellent agreement with [21, 23]. The implication of this analysis is that the double-sided L-type capacitive WPT system can be modelled as a voltage-dependent current source, I_{out}, which represents the rectified current of I_{S} as illustrated in Fig. 8. Employing the fundamental harmonic approximation [50, 51], the peak values of the currents in (11) can be found with the aid of the transconductance gain, input and output voltages as

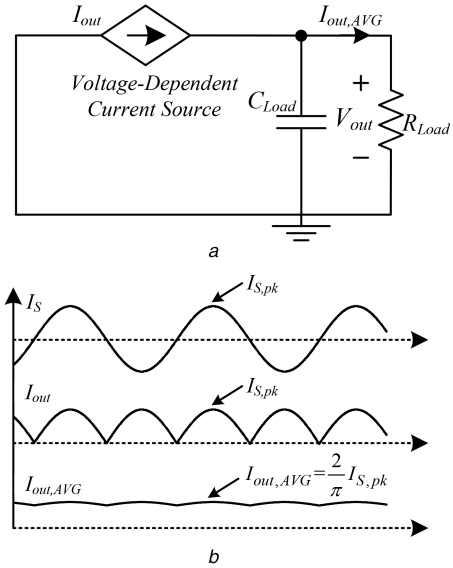

Fig. 8 *Behavioural model of the analysed capacitive WPT system for the output side*
(a) Simplified electrical circuit, ***(b)*** Secondary side currents waveforms

$$\begin{aligned} I_{\mathrm{P,pk}} &= \frac{4}{\pi}\frac{\omega_0 C_{\mathrm{P}}^* C_{\mathrm{S}}^*}{C_{\mathrm{M}}} V_{\mathrm{out}}, \\ I_{\mathrm{S,pk}} &= \frac{4}{\pi}\frac{\omega_0 C_{\mathrm{P}}^* C_{\mathrm{S}}^*}{C_{\mathrm{M}}} V_{\mathrm{in}}, \end{aligned} \tag{12}$$

and therefore the average value of the output current $I_{\mathrm{out,AVG}}$ is

$$I_{\mathrm{out,AVG}} = \frac{8}{\pi^2}\frac{\omega_0 C_{\mathrm{P}}^* C_{\mathrm{S}}^*}{C_{\mathrm{M}}} V_{\mathrm{in}}. \tag{13}$$

It should be noted that not all CPT systems can be simplified into a voltage-dependent current source. However, the presented network-based modelling approach significantly simplifies the input–output relationships of any L-type based capacitive WPT system by using the gyrator characteristics.

To verify and show a proof-of-concept of the behavioural model, a cycle-by-cycle simulation test-bench for the analysed CPT system has been constructed in PSIM (PowerSim, Inc.). The input voltage is 70 V and the medium mutual capacitance $C_{\mathrm{M}} = 6$ pF, at resonant frequency $f_0 \simeq 1.55$ MHz for a load resistance $R_{\mathrm{Load}} = 15\ \Omega$ and output capacitor $C_{\mathrm{Load}} = 200$ μF. The first set of simulations has been carried out for symmetrical matching parameters: $L_{\mathrm{P}} = L_{\mathrm{S}} = 67$ μH, $C_{\mathrm{P}}^* \simeq C_{\mathrm{P}} = C_{\mathrm{S}}^* \simeq C_{\mathrm{S}} = 156$ pF. The simulation results of the currents and voltages of the primary and secondary sides are shown in Figs. 9*a* and *b*, respectively, whereas the dashed lines show the behavioural model predictions. The obtained peak values of the currents are in good agreement with the theoretical predictions in (12), which further imply that the average output current, $I_{\mathrm{out,AVG}}$, is as expected from (13).

The second set of simulations has been carried out for asymmetrical matching parameters: $L_{\mathrm{P}} = 67$ μH, $C_{\mathrm{P}}^* \simeq C_{\mathrm{P}} = 156$ pF for the primary side, and $L_{\mathrm{S}} = 90$ μH, $C_{\mathrm{S}}^* \simeq C_{\mathrm{S}} = 116$ pF for the secondary side. Fig. 10 depicts simulation waveforms of the currents and voltages of the primary and secondary. As can be seen, the obtained results match the model predictions. It can also be noticed that the resulting output current is lower than that in the symmetrical case shown in Fig. 9. This is due to the lower transconductance gain in the case with a lower value of C_{S}.

Finally, the calculated results for the average output current of an asymmetrical case are plotted against the results obtained from the simulation. These are depicted in Fig. 11, where Fig. 11*a* shows the current as a function of the input voltage and Fig. 11*b* shows the current as a function of the coupling capacitances. A very good agreement is obtained throughout these simulations. As can be seen in Fig. 11*b*, as predicted by the model in (12), the output current is

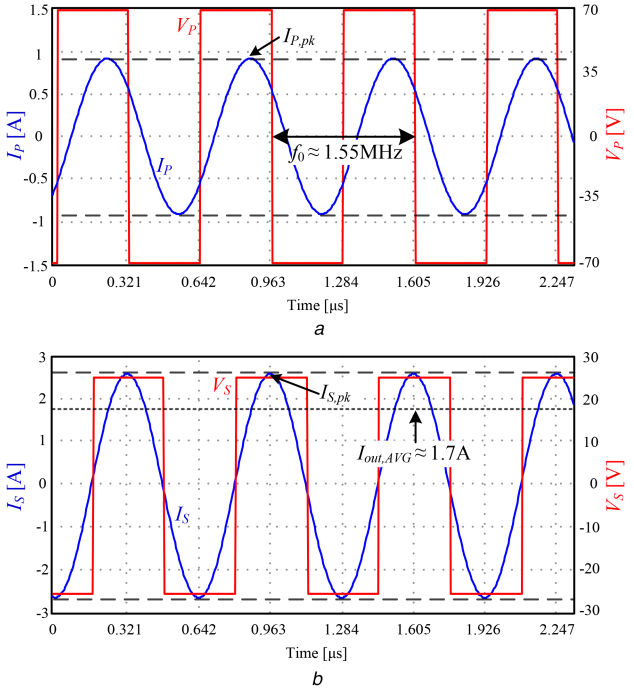

Fig. 9 *Simulated waveforms of the currents and voltages for symmetrical matching parameters (dashed lines are the behavioural model predictions)*
(a) Primary, ***(b)*** Secondary

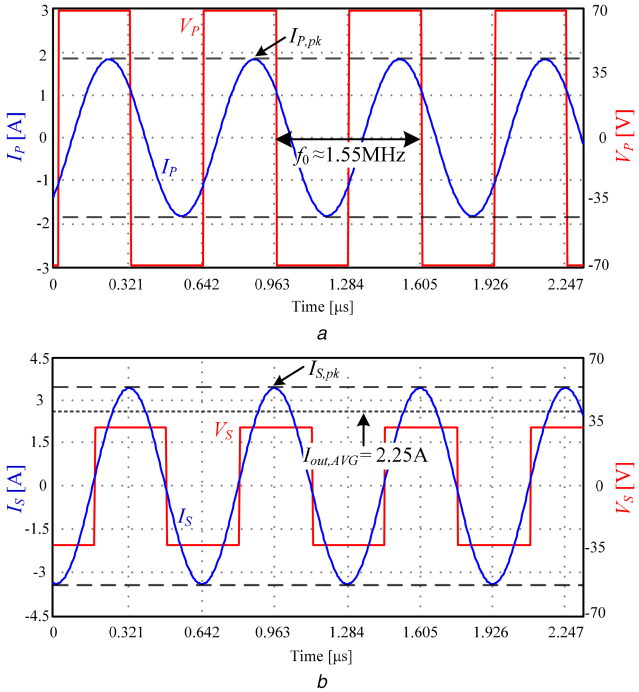

Fig. 10 *Currents and voltages simulation results for asymmetrical matching parameters (dashed lines are the behavioral model predictions)*
(a) Primary, ***(b)*** Secondary

inversely proportional to the mutual coupling capacitance C_M. Therefore, the output power will follow a similar trend.

4 Simulation-compatible capacitive medium modelling

The coupling capacitance of the medium depends on various factors such as conductors, dielectric material, alignment and distance between the coupling plates. Evaluation of a WPT system in a simulation environment for these variables over time or frequency is a major challenge since a continuous variable capacitance is required. To-date, this element is generally absent

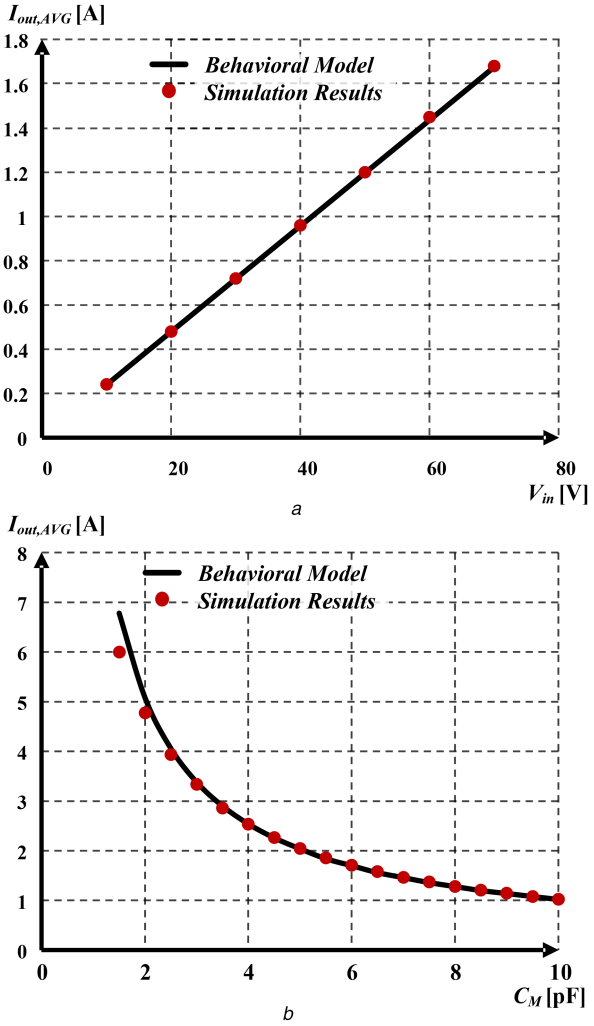

Fig. 11 *Behavioural model and simulated average output current, $I_{out,AVG}$, curves for an asymmetrical setup*
(a) As a function of the input voltage V_{in}, ***(b)*** As a function of the mutual coupling capacitance C_M

from the common simulation software packages. Methods to obtain the medium characteristics either involve rigorous and tedious experiments and/or finite element analysis [24]. However, even in cases in which these characteristics are obtained, the analysis of their interaction with the electrical circuit is still required. To this end, a continuous-time model for variable capacitors, which can be extended to a variable-capacitance network model, has been developed and implemented in the PSIM platform.

In this study, the methodology to model continuous-time variable inductance as described previously in [44, 52] has been employed and adapted to describe variable capacitance. As illustrated in Fig. 12, the model comprises two dependent voltage and current sources, which emulate a non-linear transformer, and a capacitor with a reference capacitance. The characteristics of the non-linear transformer are defined by the following relationships:

$$\begin{aligned} V_2 &= K_{cap} V_1, \\ I_2 &= I_1, \end{aligned} \tag{14}$$

where K_{cap} is the transformer's scale factor between the primary and secondary, and C_{ref} is the constant reference capacitance. From (14), the capacitive impedance reflected to the primary side, Z_C, with respect to the capacitive impedance at the secondary, Z_{Cref} is

$$\begin{cases} Z_{\rm C} = \dfrac{1}{{\rm j}\omega C} = \dfrac{V_1}{I_1} = \dfrac{V_2}{K_{\rm cap} I_2} \\ Z_{\rm Cref} = \dfrac{1}{{\rm j}\omega C_{\rm ref}} = \dfrac{V_2}{I_2} \end{cases} \Rightarrow Z_{\rm C} = \frac{1}{K_{\rm cap}} Z_{\rm Cref}, \quad (15)$$

and therefore, the capacitor value reflected to the primary side is obtained as

$$C = K_{\rm cap} C_{\rm ref}\,. \quad (16)$$

For the sake of simplicity, $C_{\rm ref}$ has been set to 1 F. In this case, the effective capacitance that is reflected across the capacitor terminals equals the scale factor $K_{\rm cap}$. To evaluate a WPT system for continuous operation, $K_{\rm cap}$ can be made dependent on system parameters such as changes in distance and/or coupling capacitance, matching network variations and mistuned resonant frequency. Thus, a voltage-dependent variable capacitor is emulated between nodes $C+$ and $C-$, as shown in Fig. 12.

Now, having a continuous-time behavioural model of a variable capacitor, the variable capacitive medium π-model of Fig. 13*a* can be created by means of three voltage-dependent voltage sources as illustrated in Fig. 13*b*, where the reference capacitances are not depicted for clarity.

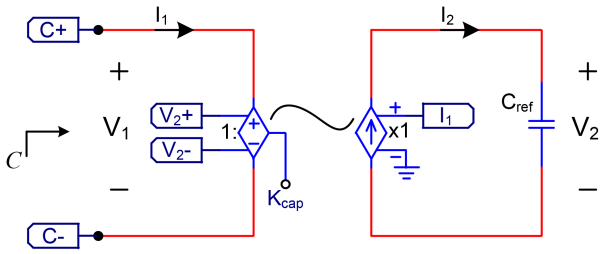

Fig. 12 *Continuous variable capacitor model in PSIM platform*

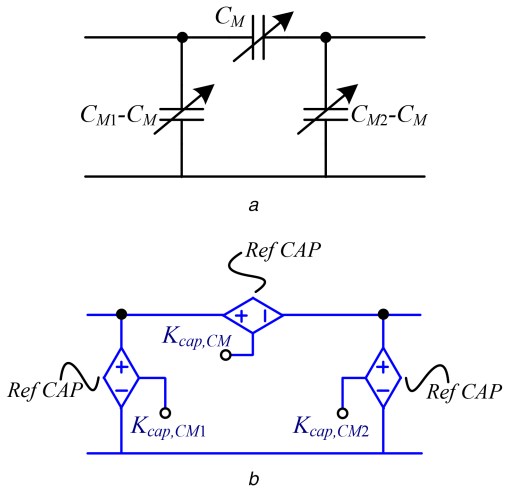

Fig. 13 *Variable capacitive medium π-model*

(a) Electrical model, ***(b)*** Representation of the variable medium by three voltage-dependent voltage sources for simulation purposes

In order to evaluate the performance of a double-sided L-type system for continuous medium (distance) variations, based on the above-presented modelling technique, a simulation test-bench with variable capacitors has been constructed as shown in Fig. 14. There, for convenience, the capacitive medium is illustrated by variable capacitor symbols. Simulations have been carried out under nominal operating conditions and matching networks that are identical to those of the asymmetrical case study in Section 3, whereas the initial coupling capacitance is 3.5 pF. Fig. 15*a* shows the result of the average value of $I_{\rm out}$ for a 1.5 pF variation of the mutual capacitance, such that the final coupling capacitance is $C_{\rm M}$ = 5 pF. The solid red line shows the simulation result, whereas the dashed blue markers show the behavioural model outcome. It can be observed that the results of the cycle-by-cycle simulation and behavioural model are in very good agreement. It can be further noticed that when $C_{\rm M}$ increases, the output current decreases as expected from the theoretical analysis. Fig. 15*b* shows the output current for a medium step-down variation of 1.5 pF, such that the final coupling capacitance is $C_{\rm M}$ = 2 pF. The output current settles on ∼5 A for both the model and cycle-by-cycle simulation, which suits well the theoretical predictions as shown in detail in Fig. 11*b*. It should be noted that since the resonant tank is operated at a significantly higher frequency than the output filter time constant ($R_{\rm Load}$ and $C_{\rm load}$), it is assumed instantaneous from a dynamic perspective (detailed dynamic analysis is beyond the scope of this study and will be detailed in upcoming subsequent publications). This is exemplified in Fig. 15 where it can be observed that the system response to step variation of $C_{\rm M}$ can be well approximated to the output filter time constant.

5 General model validation

To further validate and examine the behavioural modelling approach, an experimental double-sided L-type capacitive WPT prototype with four copper plates that form the capacitive coupling has been constructed as shown in Fig. 16. The coupling plates have been designed symmetrically, such that each plate is 25 × 25 cm. Thus, the matching networks have also been designed to be symmetrical, with $L_{\rm P} = L_{\rm S} \simeq 67$ μH and $C_{\rm P} = C_{\rm S} = 156$ pF. The gate drive signals of the full-bridge inverter were generated with a Cyclone IV field programmable gate array [53] at an operating frequency slightly above the resonance $f_0 \simeq 1.558$ MHz guaranteeing soft-switching operation. The full-bridge inverter has been implemented with GaN modules operable at several MHz [54]. To reduce the limitations due to magnetic and skin-effect losses in the MHz range [55, 56], the matching inductors $L_{\rm P}$ and $L_{\rm S}$ have been constructed with an AWG 48 litz wire wrapped on an air-core. It should be noted that the actual litz wire resistance at the operation frequency of MHz range may be different than the manufacturer specified resistance, typically at 100 kHz. High-voltage multilayer surface mount device ceramic capacitors have been used in parallel to form the desired matching capacitors $C_{\rm P}$ and $C_{\rm S}$.

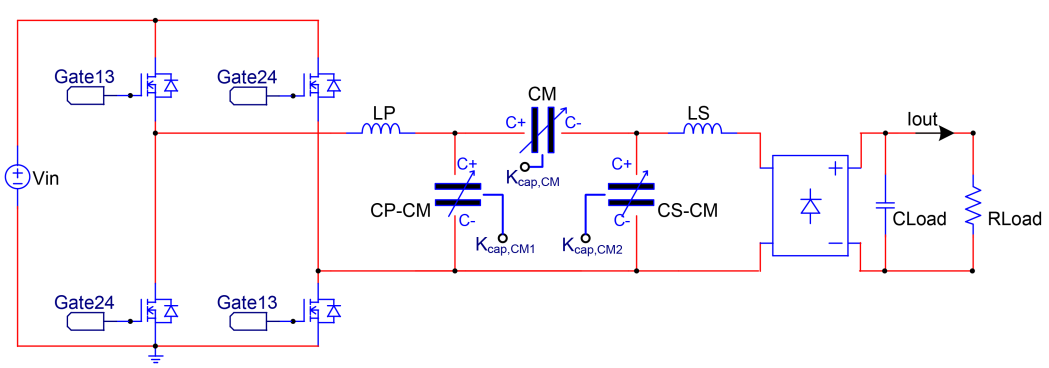

Fig. 14 *Schematic simulation test-bench of the WPT system with variable capacitor symbol illustrations for the capacitive medium*

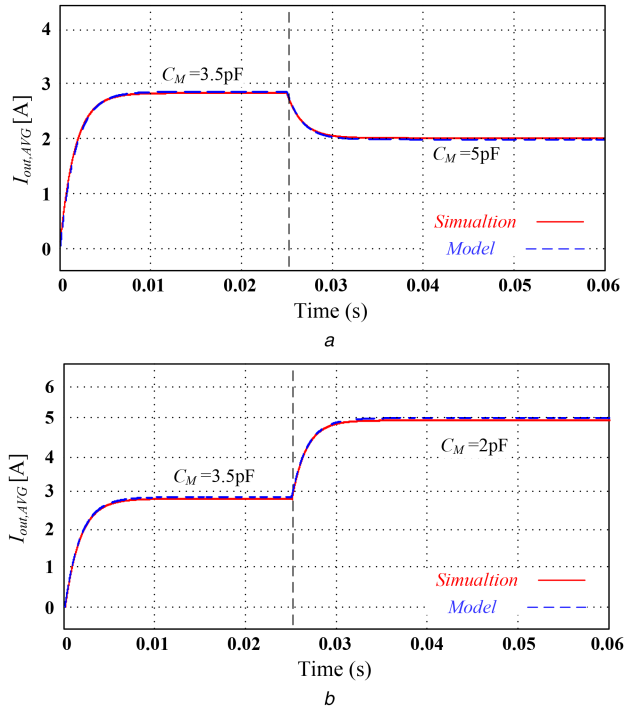

Fig. 15 *Average output current for capacitive medium variations with initial mutual capacitance C_M = 3.5 pF*

(a) Step-up of 1.5 pF, ***(b)*** Step-down of 1.5 pF

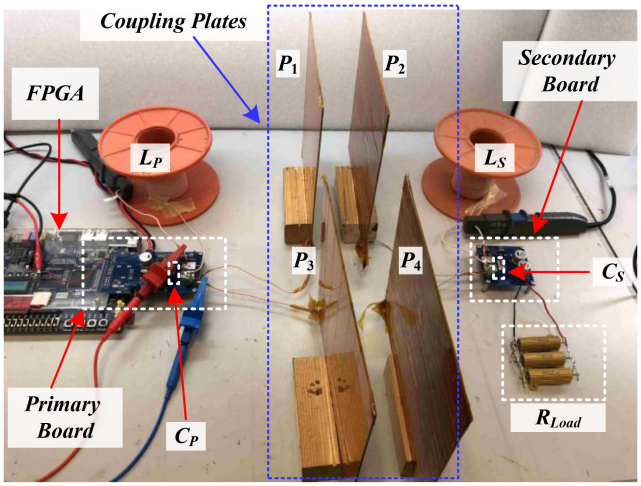

Fig. 16 *Experimental setup of a capacitive WPT prototype*

To facilitate reliable estimation of the capacitive coupler for the experimental measurements, estimation of the plate capacitance has been carried out by Maxwell (Ansys) finite element analysis tool. A rigorous simulation procedure of various dimensions and geometries has been carried out to determine the mutual capacitance, C_M, for the given coupling plates under various air-gaps (Fig. 17).

Fig. 18 shows experimental waveforms of the system for the input voltage $V_{in} = 70$ V and a load resistance $R_{Load} = 15\ \Omega$, whereas the distance between the plates is 50 mm resulting in coupling capacitance $C_M \simeq 6$ pF. Fig. 18*a* shows the primary sinusoidal current I_P, it can be noticed that the current is slightly lagging the primary voltage V_P validating soft-switching operation. The sinusoidal current at the secondary I_S is shown in Fig. 18*b*. The obtained peak value (3.4 A) and the resulting average value (~2.2 A) at the secondary are similar to the simulation results shown in Fig. 9*b* with a small error of 4%. It should be noted that although the matching network at the secondary side is not perfectly tuned to the resonant frequency due to small system parasitics, the experimental measurements tightly follow the

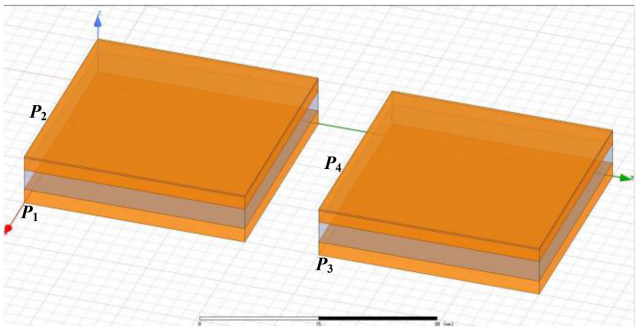

Fig. 17 *Maxwell (Ansys software) simulation test-bench for the capacitive coupler design*

behavioural model predictions. The overall operating conditions and parameters of the experimental prototype are summarised in Table 1.

To further verify the strength of the behavioural model, the average output current has been measured for various input voltages, for a constant C_M of 6 pF; the results are summarised in Fig. 19. The experimental measurements tightly follow the results obtained by the simulations as well as the model predictions. It can be noticed that the output current (as well as the output power) increases with the input voltage, as predicted from the gyrator current–voltage relationships obtained in Section 3. Fig. 20 depicts the output current comparison between an experimental, simulated and behavioural model for various air-gaps between 25 and 100 mm, which corresponds to a mutual capacitance range of ~3–10 pF, thus demonstrating variations in distance and/or displacement (while $V_{in} = 70$ V). This way, the inversely proportional behaviour between the capacitive coupling and the output current is well validated by the experimental measurements. It can be noticed that for relatively small C_M the measured current is lower than predicted, the discrepancy can be explained by the fact that beyond a certain distance the system go from near-field to far-field operation, and it behaves as an antenna rather than a coupling system. This implies that some assumptions that have been made for the behavioural model analysis are not satisfied.

6 Conclusion

A generic two-port network-based modelling approach for resonant capacitive WPT systems has been presented. Based on the modelling approach, the behaviour of a resonant-operating CPT system (or in the vicinity of resonant operation) can be analysed and described for different system variations such as capacitive coupling interface, resonant frequency and matching network components. The modelling method provides an insight into the effects of the parameters on the system behaviour, the cross-coupling relationships between transmitter and receiver sides, and source features based on the operation mode and settings. The simplicity and generality of the gyrator model as an energy transfer element offers an efficient closed-form alternative to complex analytical approaches or tedious numerical simulations. The presented behavioural model establishes the foundations for overall closed-loop analysis and controller design for capacitive WPT systems. This study also introduced a simulation-compatible variable capacitor model that is applicable for continuous-time analysis of WPT systems. This provides a simulation framework to account for variations of the capacitive medium such as coupling coefficient, dielectric material, alignment and distance between the coupling plates.

This study also introduced a simulation-compatible variable capacitor model that is applicable for continuous-time analysis of WPT systems. This provides a simulation framework to account for capacitive medium variations such as the coupling coefficient, dielectric material, alignment and distance between the coupling plates.

The behavioural model and methodology have been validated through simulation and experiments. To this end, an experimental CPT prototype operating in the MHz range has been constructed.

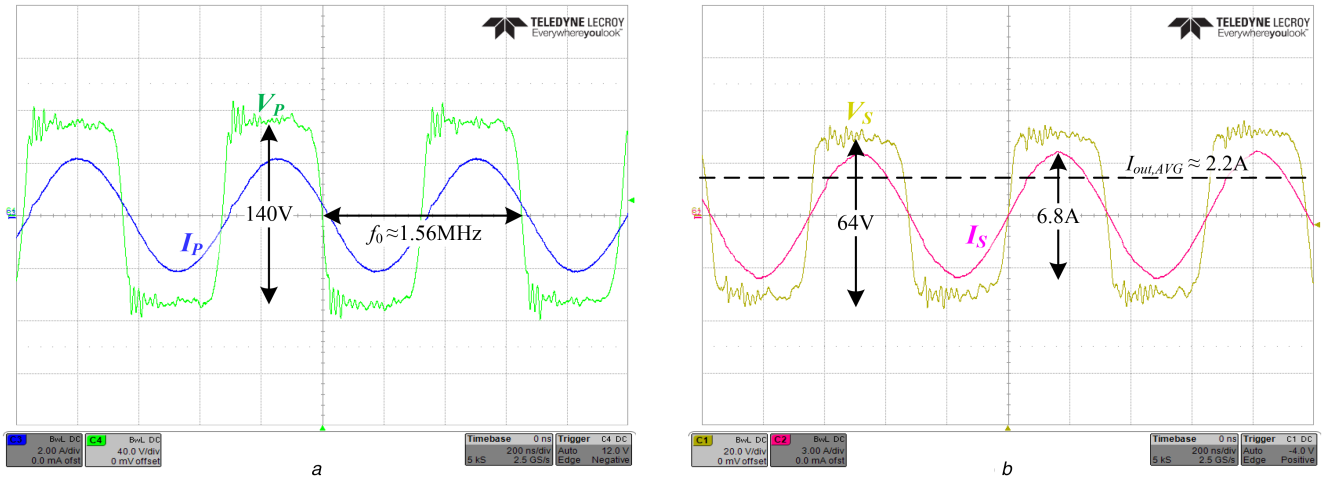

Fig. 18 *Experimental waveforms with operating conditions: V_{in} = 70 V, R_{Load} = 15 Ω, coupling capacitance $C_M \simeq 6$ pF*
(a) Primary side V_P 40 V/div, I_P 2 A/div, ***(b)*** Secondary side V_S 20 V/div, I_S 3 A/div; time scale 200 ns/div

Table 1 Experimental prototype values and parameters

Parameter	Value/type
input voltage V_{in}	70 V
output current $I_{out,AVG}$	up to 4 A
load resistance R_{Load}	15 Ω
coupling plates	25 × 25 cm
coupling capacitance C_M /air-gaps	3–10 pF/25–100 mm
full-bridge transistors	LMG5200, 80 V, dual
rectifier diodes	5 A/200 V, VSSC520S-M3
inductors L_P and L_S	~67 μH
capacitors C_P and C_S	156 pF, AVX MLLC 5 kV
output capacitor C_{Load}	200 μF, EEV-FK2A101M
resonant frequency f_0	~1.558 MHz

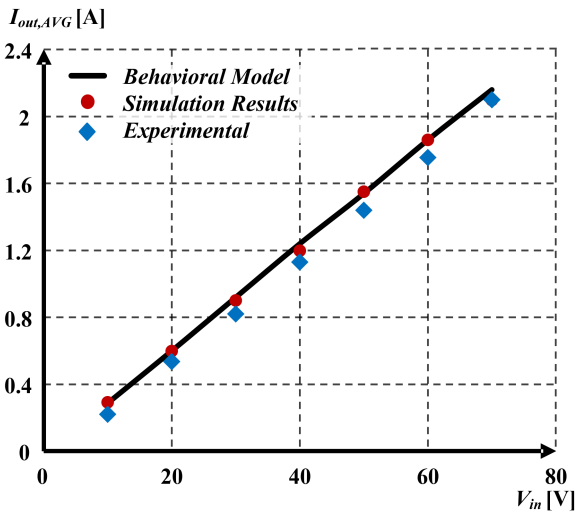

Fig. 19 *Average output current, $I_{out,AVG}$, curve as a function of the input voltage V_{in}, for 50 mm air-gap*

The prototype has been evaluated for various air-gaps up to 100 mm and 200 W output power delivery. The experimental case-study confirmed the theoretical predictions of the model with an excellent agreement between the analytical derivations, simulations, and experimental results.

7 Acknowledgment

This research was supported by the Pazi Foundation.

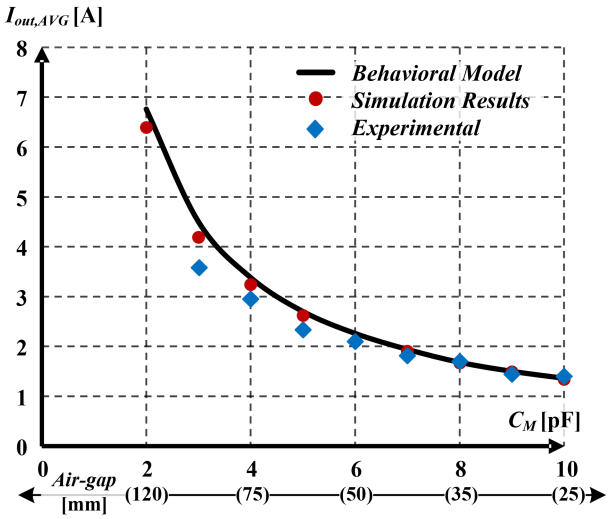

Fig. 20 *Average output current, $I_{out,AVG}$, curve as a function of the mutual coupling capacitance C_M /air-gaps, for V_{in} = 70 V*

8 References

[1] Imura, T., Hori, Y.: 'Maximizing air gap and efficiency of magnetic resonant coupling for wireless power transfer using equivalent circuit and Neumann formula', *IEEE Trans. Ind. Electron.*, 2011, **58**, (10), pp. 4746–4752

[2] Si, P., Hu, A.P., Malpas, S., *et al.*: 'A frequency control method for regulating wireless power to implantable devices', *IEEE Trans. Biomed. Circuits Syst.*, 2008, **2**, pp. 22–29

[3] Langlotz, T, Nguyen, T., Schmalstieg, D., *et al.*: 'Next generation augmented reality browsers: rich, seamless, and adaptive', *Proc. IEEE*, 2014, **102**, pp. 155–169

[4] Sallan, J., Villa, J.L., Llombart, A., *et al.*: 'Optimal design of ICPT systems applied to electric vehicle battery charge', *IEEE Trans. Ind. Electron.*, 2009, **56**, (6), pp. 2140–2149

[5] Yin, D., Oh, S., Hori, Y.: 'A novel traction control for EV based on maximum transmissible torque estimation', *IEEE Trans. Ind. Electron.*, 2009, **56**, (6), pp. 2086–2094

[6] Zhang, W., Zhang, T., Guo, Q., *et al.*: 'High-efficiency wireless power transfer system for 3D, unstationary free-positioning and multi-object charging', *IET Electr. Power Appl.*, 2018, **12**, (5), pp. 658–665

[7] Kamiya, Y., Nakamura, T., Sato, T., *et al.*: 'Development and performance evaluation of advanced electric micro bus equipped with non-contact inductive rapid-charging system'. Proc. 23rd Int. EVS, Electric/Hybrid-Electric Session, Anaheim, CA, USA, 2007, pp. 1–14

[8] Mostefai, L., Denai, M., Sehoon, O., *et al.*: 'Optimal control design for robust fuzzy friction compensation in a robot joint', *IEEE Trans. Ind. Electron.*, 2009, **56**, (10), pp. 3832–3839

[9] Xu, D., Han, L., Tan, M., *et al.*: 'Ceiling-based visual positioning for an indoor mobile robot with monocular vision', *IEEE Trans. Ind. Electron.*, 2009, **56**, (5), pp. 1617–1628

[10] Bingyi, Z., Hongbin, L., Yisong, Z., *et al.*: 'Contactless electrical energy transmission system using separable transformer'. Proc. 8th Int. Conf. on Electrical Machines and Systems, Nanjing, China, 2005, vol. 3, pp. 1721–1724

[11] Li, S., Mi, C.: 'Wireless power transfer for electric vehicle applications', *IEEE J. Emerging Sel. Top. Power Electron.*, 2014, **3**, (1), pp. 4–17
[12] Jaegue, S., Seungyong, S., Yangsu, K., *et al.*: 'Design and implementation of shaped magnetic resonance-based wireless power transfer system for roadway-powered moving electric vehicles', *IEEE Trans. Ind. Electron.*, 2014, **61**, (3), pp. 1179–1192
[13] Wu, K., Choudhury, D., Matsumoto, H.: 'Wireless power transmission, technology, and applications', *Proc. IEEE*, 2013, **101**, pp. 1271–1275
[14] Collins, L.: 'Cut the cord', *IET J. Mag.*, 2007, **5**, (6), pp. 42–46
[15] Valente, V., Eder, C., Donaldson, N., *et al.*: 'A high-power CMOS class-D amplifier for inductive link medical transmitters', *IEEE Trans. Power Electron.*, 2015, **30**, (8), pp. 4477–4488
[16] Hui, S.Y.R., Zhong, W., Lee, C.K.: 'A critical review of recent progress in mid-range wireless power transfer', *IEEE Trans. Power Electron.*, 2014, **29**, (9), pp. 4500–4511
[17] Musavi, F., Eberle, W.: 'Overview of wireless power transfer technologies for electric vehicle battery charging', *IET Power Electron.*, 2014, **7**, (1), pp. 60–66
[18] Theodoridis, M.P.: 'Effective capacitive power transfer', *IEEE Trans. Power Electron.*, 2012, **27**, (12), pp. 4906–4913
[19] Lu, F., Zhang, H., Hofmann, H., *et al.*: 'A double-sided LCLC compensated capacitive power transfer system for electric vehicle charging', *IEEE Trans. Power Electron.*, 2015, **30**, (11), pp. 6011–6014
[20] Zhang, H., Lu, F., Hofmann, H., *et al.*: 'A four-plate compact capacitive coupler design and LCL-compensated topology for capacitive power transfer in electric vehicle charging application', *IEEE Trans. Power Electron.*, 2016, **31**, (12), pp. 8541–8551
[21] Lu, F., Zhang, H., Hofmann, H., *et al.*: 'A loosely coupled capacitive power transfer system with LC compensation circuit topology'. Proc. IEEE Energy Conversion Congress and Exposition (ECCE), Milwaukee, WI, USA, 2016, pp. 1–5
[22] Lu, F., Zhang, H., Mi, C.: 'A two-plate capacitive wireless power transfer system for electric vehicle charging applications', *IEEE Trans. Power Electron.*, 2017, **33**, (2), pp. 946–969
[23] Lu, F., Zhang, H., Hofmann, H., *et al.*: 'A double-sided LC compensation circuit for loosely-coupled capacitive power transfer', *IEEE Trans. Power Electron.*, 2017, **33**, (2), pp. 1633–1643
[24] Dai, J., Ludois, D.C.: 'A survey of wireless power transfer and a critical comparison of inductive and capacitive coupling for small gap applications', *IEEE Trans. Power Electron/*, 2015, **30**, (11), pp. 6017–6029
[25] Lu, F., Zhang, H., Hofmann, H., *et al.*: 'An inductive and capacitive integrated coupler and its LCL compensation circuit design for wireless power transfer', *IEEE Trans. Ind. Appl.*, 2017, **53**, (5), pp. 4903–4913
[26] Lim, Y., Tang, H., Lim, S., *et al.*: 'An adaptive impedance-matching network based on a novel capacitor matrix for wireless power transfer', *IEEE Trans. Power Electron.*, 2014, **29**, (8), pp. 4403–4413
[27] Beh, T.C., Kato Imura, M.T., Oh, S., *et al.*: 'Automated impedance matching system for robust wireless power transfer via magnetic resonance coupling', *IEEE Trans. Ind. Electron.*, 2013, **60**, (9), pp. 3689–3698
[28] Zhang, W., Mi, C.: 'Compensation topologies for high power wireless power transfer systems', *IEEE Trans. Veh. Technol.*, 2015, **65**, (6), pp. 4768–4778
[29] Sinha, S., Kumar, A., Pervaiz, S., *et al.*: 'Design of efficient matching networks for capacitive wireless power transfer systems'. Proc. IEEE Workshop on Control and Modeling for Power Electronics (COMPEL), Trondheim, Norway, 2016, pp. 1–7
[30] Kumar, A., Sinha, S., Sepahvand, A., *et al.*: 'Improved design optimization for high-efficiency matching networks', *IEEE Trans. Power Electron.*, 2018, **33**, (1), pp. 37–50
[31] Pantic, Z., Sanzhong, B., Lukic, S.: 'ZCS LCC-compensated resonant inverter for inductive-power-transfer application', *IEEE Trans. Ind. Electron.*, 2011, **58**, (9), pp. 3500–3510
[32] Witulski, A., Erickson, R.W.: 'Extension of state-space averaging to resonant switches and beyond', *IEEE Trans. Power Electron.*, 1990, **5**, (1), pp. 98–109
[33] Hao, H., Covic, G.A., Boys, J.T.: 'An approximate dynamic model of LCL-T-based inductive power transfer power supplies', *IEEE Trans. Power Electron.*, 2014, **29**, (10), pp. 5554–5567
[34] Vorperian, V., Tymerski, R., Lee, F.C.: 'Equivalent circuit models for resonant and PWM switches', *IEEE Trans. Power Electron.*, 1989, **4**, (2), pp. 205–214
[35] Maksimovic, D., Cuk, S.: 'A unified analysis of PWM converters in discontinuous modes', *IEEE Trans. Power Electron.*, 1991, **6**, (3), pp. 476–490
[36] Lu, J., Kumar, A., Afridi, K.K.: 'A step-superposition based analysis approach to modeling resonant converters', *IEEE Trans. Power Electron.*, 2018, **33**, (8), pp. 7148–7165
[37] Anderson, C.J., Lyle, J.A.: 'Technique for evaluating system performance using Q in numerical simulation exhibiting inter symbol interference', *Electron. Lett.*, 1994, **30**, (1), pp. 71–72
[38] Chen, L., Liu, S., Zhou, Y., *et al.*: 'An optimizable circuit structure for high-efficiency wireless power transfer', *IEEE Trans. Ind. Electron.*, 2013, **60**, (1), pp. 339–349
[39] Wang, B., Yerazunis, W., Teo, K.H.: 'Wireless power transfer: metamaterials and array of coupled resonators', *Proc. IEEE*, 2013, **101**, pp. 1359–1368
[40] Christ, A., Douglas, M.G., Roman, J.M., *et al.*: 'Evaluation of wireless resonant power transfer systems with human electromagnetic exposure limits', *IEEE Trans. Electromagn. Compat.*, 2013, **55**, (2), pp. 265–274
[41] Yuan, Q., Chen, Q., Li, L., *et al.*: 'Numerical analysis on transmission efficiency of evanescent resonant coupling wireless power transfer system', *IEEE Trans. Antennas Propag.*, 2010, **58**, (5), pp. 1751–1758
[42] Cheon, S., Kim, Y.H., Kang, S.Y., *et al.*: 'Circuit-model-based analysis of a wireless energy-transfer system via coupled magnetic resonances', *IEEE Trans. Ind. Electron.*, 2011, **58**, (7), pp. 2906–2914
[43] Lin, C., Lee, F.: 'Design of a piezoelectric transformer converter and its matching networks'. Proc. IEEE Power Electronics Specialist Conf. (PESC'94), Taipei, Taiwan, 1994, vol. 1, pp. 607–612
[44] Evzelman, M., Peretz, M.M.: 'Optimal design of a class-E resonant driver', *IET Power Electron.*, 2015, **8**, (8), pp. 1552–1557
[45] Sohn, Y.H., Choi, B.H., Cho, G.H., *et al.*: 'Gyrator-based analysis of resonant circuits in inductive power transfer systems', *IEEE Trans. Power Electron.*, 2016, **31**, (10), pp. 6824–6843
[46] Cid-Pastor, A., Martinez-Salamero, L., Alonso, C., *et al.*: 'Paralleling DC–DC switching converters by means of power gyrators', *IEEE Trans. Power Electron.*, 2007, **22**, (6), pp. 2444–2453
[47] Hamill, D.C.: 'Lumped equivalent circuits of magnetic components: the gyrator–capacitor approach', *IEEE Trans. Power Electron.*, 1993, **8**, (2), pp. 97–103
[48] Singer, S.: 'Loss-free gyrator realization', *IEEE Trans. Circuits Syst.*, 1988, **35**, (1), pp. 26–34
[49] Singer, S.: 'Gyrators application in power processing circuits', *IEEE Trans. Ind. Electron.*, 1987, **IE-34**, (3), pp. 313–318
[50] Steigerwald, R.L.: 'A comparison of half-bridge resonant converter topologies', *IEEE Trans. Power Electron.*, 1988, **3**, (2), pp. 174–182
[51] Hayes, J.G., Egan, M.G.: 'Rectifier-compensated fundamental mode approximation analysis of the series parallel LCLC family of resonant converters with capacitive output filter and voltage-source load'. Proc. IEEE Power Electronics Specialists Conf. (PESC), Charleston, SC, USA, 1999, vol. 2, pp. 1030–1036
[52] Ben-Yaakov, S., Peretz, M.M.: 'Simulation bits: a SPICE behavioral model of non-linear inductors', *IEEE Power Electron. Soc. Newslett, Fourth Quarter*, 2003, **15**, (4), pp. 9–10
[53] DE2 development and education board user manual, Altera Corporation, 2006
[54] Texas Instrument: 'LMG5200 80-V, 10-A GaN half-bridge power stage'. Available at http://www.ti.com/lit/ds/symlink/lmg5200.pdf, accessed March 2017
[55] Craninckx, J., Steyaert, M.: 'A 1.8-GHz low-phase-noise CMOS VCO using optimized hollow spiral inductors', *IEEE J. Solid-State Circuits*, 1997, **32**, (5), pp. 736–744
[56] Bartoli, M., Noferi, N., Reatti, A., *et al.*: 'Modeling Litz-wire winding losses in high-frequency power inductors'. Proc. IEEE Power Electronics Specialists Conf., Baveno, Italy, 1996, vol. 2, pp. 1690–1696

9 Appendix

This appendix details the analytical derivations and observations required in Section 2.2, to extract the input–output characteristics of the matching networks that have been surveyed earlier. This provides a network perspective to the interaction between the source and load sides.

The relationship of the voltage and current of a series–parallel LC matching structure (Fig. 3*a*) can be expressed as

$$\begin{cases} V_{\mathrm{P}_1} = \mathrm{j}\omega L_{\mathrm{P}} I_{\mathrm{P}_1} + V_{\mathrm{P}_2} \\ V_{\mathrm{P}_2} = \dfrac{1}{\mathrm{j}\omega C_{\mathrm{P}}}(I_{\mathrm{P}_1} - I_{\mathrm{P}_2}) \end{cases} \Rightarrow \begin{cases} I_{\mathrm{P}_1} = \dfrac{(V_{\mathrm{P}_1} - V_{\mathrm{P}_2})}{\mathrm{j}\omega L_{\mathrm{P}}}, \\ V_{\mathrm{P}_1} = \mathrm{j}\omega L_{\mathrm{P}} I_{\mathrm{P}_1} + \dfrac{1}{\mathrm{j}\omega C_{\mathrm{P}}}(I_{\mathrm{P}_1} - I_{\mathrm{P}_2}). \end{cases} \tag{17}$$

Assuming that the switching frequency equals the resonant frequency, the currents $I_{\mathrm{P}1}$ and $I_{\mathrm{P}2}$ are given by

$$\begin{cases} I_{\mathrm{P}_1} = -j\omega_0 C_{\mathrm{P}}(V_{\mathrm{P}_1} - V_{\mathrm{P}_2}); \\ I_{\mathrm{P}_2} = -\mathrm{j}\omega_0 C_{\mathrm{P}} V_{\mathrm{P}_1}; \end{cases} \quad \omega_0 L_{\mathrm{P}} = \frac{1}{\omega_0 C_{\mathrm{P}}}, \tag{18}$$

where ω_0 is the resonant angular frequency.

By modifying the L-type network in Fig. 3*a* with an additional series resonator, a T-type network (L_{P}–C_{P}–L_{P}*) is obtained as shown in Fig. 3*b*. At the resonant frequency, this modification is effectively a short circuit, and the resulting T-type network has the characteristics of a gyrator as follows:

$$\begin{aligned} V_{\mathrm{P}_1} &= \mathrm{j}\omega_0 L_{\mathrm{P}} I_{\mathrm{P}_1} + \frac{1}{\mathrm{j}\omega_0 C_{\mathrm{P}}}(I_{\mathrm{P}_1} - I_{\mathrm{P}_2}) = \frac{1}{-\mathrm{j}\omega_0 C_{\mathrm{P}}} I_{\mathrm{P}_2}, \\ V_{\mathrm{P}_2}^{*} &= -\mathrm{j}\omega_0 L_{\mathrm{P}} I_{\mathrm{P}_2} + \frac{1}{\mathrm{j}\omega_0 C_{\mathrm{P}}}(I_{\mathrm{P}_1} - I_{\mathrm{P}_2}) = \frac{1}{\mathrm{j}\omega_0 C_{\mathrm{P}}} I_{\mathrm{P}_1}, \end{aligned} \tag{19}$$

it should be noted that without losing generality, (19) can be expressed in a matrix representation as

$$\begin{bmatrix} I_{P1} \\ I_{P2} \end{bmatrix} = \begin{bmatrix} 0 & \underbrace{j\omega_0 C_P}_{-G} \\ \underbrace{-j\omega_0 C_P}_{G} & 0 \end{bmatrix} \begin{bmatrix} V_{P1} \\ V_{P2}^* \end{bmatrix}. \tag{20}$$

The current I_{P2} can also be expressed as

$$I_{P2} = j\omega_0 C_P (V_{P2}^* - V_{P2}). \tag{21}$$

Rearranging (20) and (21), and after some manipulations, the voltage V_{P2}* can be written as

$$V_{P2}^* = V_{P2} - V_{P1}, \tag{22}$$

substituting (22) into (20) results in the same value of the current I_{P1} as given in (18). This implies that the initial current–voltage relationships of the series–parallel LC matching network are preserved through a gyrator or two-port network representation. From the gyrator characteristics and under the constraint of operating at the resonant frequency, Fig. 3*b* can be further modified by reflecting the capacitor C_P* to the first port as an inductor L_P* as depicted in Fig. 3*c*. The original current–voltage relationships shown in (18) can be obtained by applying Kirchhoff's voltage and current laws. This yields

$$\begin{cases} V_{P2} = -j\omega_0 L_P I_{P2} + \dfrac{1}{j\omega_0 C_P}(I_{P1}^* - I_{P2}) \Rightarrow I_{P1}^* = j\omega_0 C_P V_{P2}, \\ V_{P1} = -j\omega_0 L_P I_{P1}^* + \dfrac{1}{j\omega_0 C_P}(I_{P1}^* - I_{P2}) \Rightarrow I_{P2} = -j\omega_0 C_P V_{P1}, \\ I_{P1} = \dfrac{V_{P1}}{j\omega_0 L_P} + I_{P1}^* = -j\omega_0 C_P (V_{P1} - V_{P2}). \end{cases} \tag{23}$$

Then, the series–parallel LC matching circuit in Fig. 3*a* can be simplified and represented equivalently with a two-port network by a gyrator element, whereas the transconductance gain is $G = -j\omega_0 C_P$, as shown in Fig. 3*d*.

In a similar manner to the series–parallel LC matching network, the voltage and current relationships of a parallel–series LC matching structure (Fig. 4*a*) are derived as

$$\begin{cases} V_{S1} = \dfrac{(I_{S1} - I_{S2})}{j\omega C_S} \\ V_{S2} = V_{S1} - j\omega L_S I_{S2} \end{cases} \Rightarrow \begin{cases} I_{S2} = \dfrac{(V_{S1} - V_{S2})}{j\omega L_S}, \\ V_{S2} = \dfrac{(I_{S1} - I_{S2})}{j\omega C_S} - j\omega L_S I_{S2}, \end{cases} \tag{24}$$

and when operating at the resonant frequency, the currents I_{S1} and I_{S2} are expressed as

$$\begin{cases} I_{S1} = j\omega_0 C_S V_{S2}; \\ I_{S2} = -j\omega_0 C_S (V_{S1} - V_{S2}); \end{cases} \quad \omega_0 L_S, = \frac{1}{\omega_0 C_S}. \tag{25}$$

The L-type network in Fig. 4*a* can be modified by adding a parallel resonator, whereas L_S* = L_S and C_S* = C_S (Fig. 4*b*). Similarly to the case of the series branch, the parallel resonator is effectively an open circuit when operating at resonance and does not change the original characteristics of the circuit in Fig. 4*a*. By applying Kirchhoff's current law on the obtained π-type network (C_S–L_S–C_S*), a two-port network with gyrator characteristics is obtained as follows:

$$\begin{aligned} I_{S1} &= j\omega_0 C_S V_{S1} + \frac{(V_{S1} - V_{S2})}{j\omega L_S} = \underbrace{j\omega_0 C_S V_{S2}}_{-G}, \\ I_{S2}^* &= -j\omega_0 C_S V_{S2} + \frac{(V_{S1} - V_{S2})}{j\omega_0 L_S} = \underbrace{-j\omega_0 C_S V_{S1}}_{G}, \end{aligned} \tag{26}$$

or in a matrix representation

$$\begin{bmatrix} I_{S1} \\ I_{S2}^* \end{bmatrix} = \begin{bmatrix} 0 & j\omega_0 C_S \\ -j\omega_0 C_S & 0 \end{bmatrix} \begin{bmatrix} V_{S1} \\ V_{S2} \end{bmatrix}. \tag{27}$$

The current I_{S2} can be obtained with the aid of I_{S2}* from (26) as follows:

$$\begin{aligned} I_{S2} &= I_{S2}^* - \frac{V_{S2}}{j\omega L_s} \\ &= -j\omega_0 C_S V_{S1} + j\omega_0 C_S V_{S2} = -j\omega_0 C_S (V_{S1} - V_{S2}). \end{aligned} \tag{28}$$

From (26) and (28) it can be observed that the original current–voltage relationships of the parallel–series LC matching network are preserved while using a gyrator element. The latter implies that the circuit in Fig. 4*a* can be simply transformed to the circuit in Fig. 4*c*.

The LCL π-type network shown in Fig. 5*a* can also be analysed and represented by a two-port model. In resonant operation, the input and output currents can be obtained similarly to the analysis of the capacitor–inductor–capacitor (CLC) π-type network as given in (26), which can be expressed as follows:

$$\begin{aligned} I_{S1} &= \frac{V_{S1}}{j\omega_0 L_S} + (V_{S1} - V_{S2}) j\omega_0 C_S = \underbrace{-j\omega_0 C_S V_{S2}}_{-G}, \\ I_{S2} &= \frac{V_{S2}}{j\omega_0 L_S} + (V_{S1} - V_{S2}) j\omega_0 C_S = \underbrace{j\omega_0 C_S V_{S1}}_{G}, \end{aligned} \tag{29}$$

and in a matrix representation describing Fig. 5*b* as

$$\begin{bmatrix} I_{S1} \\ I_{S2} \end{bmatrix} = \begin{bmatrix} 0 & -j\omega_0 C_S \\ j\omega_0 C_S & 0 \end{bmatrix} \begin{bmatrix} V_{S1} \\ V_{S2} \end{bmatrix}. \tag{30}$$